Development of a potential energy surface for the O_3--Ar system: Rovibrational states of the complex

Journal:	*Physical Chemistry Chemical Physics*
Manuscript ID	CP-ART-02-2019-001044.R1
Article Type:	Paper
Date Submitted by the Author:	08-Mar-2019
Complete List of Authors:	Sur, Sangeeta; Missouri University of Science and Technology, Chemistry Quintas-Sánchez, Ernesto; Missouri University of Science and Technology Ndengué, Steve; Missouri University of Science and Technology, Chemistry Dawes, Richard; Missouri University of Science and Technology, Chemistry

Development of a potential energy surface for the O_3–Ar system: Rovibrational states of the complex

Sangeeta Sur, Ernesto Quintas-Sánchez, Steve A. Ndengué, and Richard Dawes*

Department of Chemistry, Missouri University of Science & Technology, Rolla, MO 65401, USA

E-mail: dawesr@mst.edu

Abstract

The cycle of formation and destruction of ozone is an important process in the atmosphere. A key step in the formation process is the stabilization of a metastable ozone molecule, which occurs through energy transfer: usually a highly excited ozone molecule loses the excess energy through inelastic collisions with a third body (M). However, the details of this energy transfer mechanism are still not well known and one of the reasons has been the lack of an accurate potential energy surface (PES). In theoretical studies, Ar is often selected as the third body when considering O_3–M dynamics. However, electronic structure calculations have not previously been reported for the complex. In this paper we benchmark the electronic structure for this system, and present our first steps towards constructing a fully flexible 6D PES by obtaining a 3D PES in the rigid rotor approximation. For this purpose, to benchmark the non-bonded interactions, we performed *ab initio* electronic structure calculations using explicitly-correlated coupled cluster theory extended to the complete basis set limit (CCSD(T)-F12b/CBS). A multireference-based protocol suitable to describe the 6D

flexible system was developed using the explicitly-correlated multi-reference configuration interaction (MRCI–F12) method. Subsequently, we used the AUTOSURF code to construct 3D PESs for each of the two methods with global root mean square errors of less than 1 cm^{-1}. The PES is characterized by two equivalent wells on either face of the ozone molecule consistent with the symmetry of the system. Calculations of the rovibrational levels for the complex using the Multiconfigurational Time Dependent Hartree (MCTDH) method provide insight into the states and dynamics of the system. Based on symmetry analysis, the allowed states and transitions were obtained: the transition frequencies and calculated rotational constants were then compared with previously reported experimental measurements. The isotopic effect was also studied using the $^{16}O^{18}O^{16}O$ and $^{16}O^{16}O^{18}O$ isotopologues. Roughly a doubling in the density of allowed states is observed when the symmetry of the ozone molecule is broken.

Introduction

Ozone is an important constituent of the atmosphere, either as a pollutant in the troposphere (lower atmosphere) or protecting life from harmful solar UV radiation passing through the stratosphere (upper atmosphere). In 1930, Chapman proposed a cycle for the formation and destruction processes:[1]

$$O_2 + h\nu \longrightarrow O + O \tag{1}$$

$$O + O + M \longrightarrow O_2 + M \tag{2}$$

$$O_2 + O + M \longrightarrow O_3^* + M \longrightarrow O_3 + M^* \tag{3}$$

$$O_3 + h\nu \longrightarrow O_2 + O \tag{4}$$

$$O_3 + O \longrightarrow 2\,O_2 \tag{5}$$

In addition to the formation and destruction processes listed here, ozone is also involved in reactive chemistry with many other species.[2–5]

There are three stable isotopes of oxygen in the atmosphere: ^{16}O (99.76%), ^{17}O (0.038%) and ^{18}O (0.205%). We will follow a common convention for notation and refer to isotopologues such as $^{16}O^{18}O^{16}O$ and $^{16}O^{16}O^{18}O$ as 686 and 668 respectively. In the early 1980s, Mauersberger[6,7] and Thiemens *et al.*[8] observed an enhancement of almost 10% of heavy ozone (in equal amounts of ^{17}O and ^{18}O) in the atmosphere (troposphere and stratosphere). This is known as the "mass-independent fractionation" (MIF) of ozone, or the "ozone isotopic anomaly." Further studies to understand the dynamics of this reaction were reported,[9,10] but it was not until 1990 that Mauersberger *et al.*[11–15] measured experimentally the rate coefficients of all the isotopes, tracing the main contribution to the anomalous isotopic selectivity to the "recombination process" occurring in step 3 shown above. The other processes, and in particular the photodissociation of ozone, lead instead to a mass-dependent fractionation of ozone.[16–22] Mauersberger *et al.* also observed that the isotope effect was independent of the identity of the third body M.[23,24] The third body M could be any species which could stabilize the sufficiently long-lived rovibrational metastable states of ozone—*i.e.*, O_3^* in step 3—after collision. The lack of any dramatic effect of the identity of the third body on collisional energy transfer, including comparisons between atomic and diatomic colliders, has also been predicted theoretically.[25]

The process of collisional stabilization of O_3^* is influenced by mass, symmetry, and nuclear spin-statistics.[26] The formation of heavier and asymmetric isotopologues of ozone is favored over the symmetric lighter ones.[10,27] To account for the isotope effect, the combined effect of two relevant factors has been cited as a partial explanation. The "zero point energy," or ΔZPE-effect,[28–31] can account for a clear trend in the formation rates of the asymmetric isotopologues; while the symmetry influence, or "η-effect,"[32–35] is the name given to a relative shift in the rates for the symmetric isotopologues. Although these two effects are not able to perfectly predict the isotope anomaly effect even today,[31] it is certainly true that these are important contributions. In particular, it is noted that there is roughly double the density of rovibrational states observable in asymmetric ozone compared with symmetric

ozone, mainly due to considerations of symmetry and nuclear spin-statistics. This is similar to the well-known and related case of $^{16}O_2$ (in its ground electronic state), for which only rotational levels with odd quantum number J exist, whereas for $^{16}O^{18}O$ all rotational levels exist. This could be highly relevant to the ozone stabilization process since the density of states can strongly influence inelastic scattering cross-sections which are often approximated by exponential gap based models.[36–38]

The recombination/exchange reaction can be written as a three step process:

$$O_2 + O + M \longrightarrow O_3^* + M \tag{6}$$

$$^yO^zO + {}^xO \longrightarrow O_3^* \longrightarrow {}^xO^zO + {}^yO \quad \text{or} \quad {}^yO^xO + {}^zO \tag{7}$$

$$O_3^* + M \longrightarrow O_3 + M^* \tag{8}$$

As mentioned earlier, the isotope selectivity was traced back to the recombination process by Mauersberger *et al.* To explain the ozone isotope anomaly, previous experimental[22,39,40] and theoretical[41,42] studies have focused primarily on the exchange process: step (7). Studies of the reaction dynamics have focused on the energy transfer (ET) mechanism of the recombination process since the 1970s. Many explanations based on classical[43–47] and quantum[48–51] dynamics have been put forward, but a quantitative prediction of all observed behavior is still missing. Recently, a mixed classical/quantum treatment approach was developed and also applied to study the ET process in ozone,[52–55] but again, quantitative agreement is still lacking. Although it is not yet known how sensitive the dynamics are to the accuracy of the interaction potential with the third body, it is noteworthy that the potential energy surfaces (PESs) used in previous studies of the ET mechanism were pairwise additive,[56] and in addition to the limitations of that simple form, they are also quite inaccurate in terms of basic parameters such as the well-depth (underrepresenting the well-depth by more than a factor of four).

In order to fully understand the recombination process, a study of the complete dynamics

(*i.e.*, exchange and stabilization processes) is necessary. The exchange process has been studied extensively[41] and accurate PESs exist[57,58] for this step. However, an accurate PES needed to study the transfer of energy from metastable ozone to the third body is lacking. The focus of a forthcoming series of papers is studying step (8) and gaining insight into the recombination process. The first step, that we present here, is the construction of an accurate interaction PES for this system. The third body M taken here is the argon (Ar) atom due to its inert nature and comparable mass to that of ozone. Details for the electronic structure of O_3–Ar and characteristics of the interaction have not yet been reported.

In this paper, we benchmark the electronic structure for the O_3–Ar system in the rigid rotor approximation, keeping the structural parameters of the ozone molecule fixed at their equilibrium position. Rovibrational calculations using the Multiconfigurational Time Dependent Hartree (MCTDH) method were performed using the constructed PESs, and compared with previously reported microwave experiments. The results from these calculations confirm the accuracy of the constructed PESs and hence the levels of underlying electronic structure theory. The PESs for two other isotopologues of ozone (*i.e.*, 686 and 668 O_3–Ar) are also constructed and the rovibrational calculations of the bound states of the two systems provide valuable insights into their nature.

Method

Ozone colliding with an argon atom is a 6D problem in full-dimensionality, with three dimensions coming from the intramolecular coordinates—bond lengths (r_1, r_2) and bond angle (α) of ozone—while the other three dimensions come from the intermolecular coordinates of the system. For the description of the non-bonded interactions between two rigid closed-shell molecules, coupled-cluster theory has proven to be straightforward to implement, robustly convergent, and highly accurate.[59–62] For studies of the spectroscopy and dynamics in vdW clusters, the rigid monomer approximation is remarkably accurate. This issue was explored

systematically by Garberoglio *et al.*[63] Although in order to obtain accurate interaction energies basis-set completeness is usually important, and core-correlation can play a role, only rarely are correlation treatments beyond perturbative triples—such as CCSDT(Q) instead of CCSD(T)—needed.[64] When large amplitude flexibility of one or more of the interacting fragments is desired, an additional challenge is presented. A correct description of significant distortions of a molecule may require a multireference electronic structure method. Although ozone is known for its multireference character,[65] it is actually reasonably well-described by single-reference methods at the equilibrium geometry where the T_1-diagnostic is only 0.023. Multireference methods such as MRCI can be less straightforward to implement, and less robustly convergent, due for example to issues relating to switches of character and orbitals flipping into/out-of the active space.[61] In addition, affordable schemes to capture high-order dynamic electron correlation (important for an accurate description of non-bonded interactions) are still lacking for these methods. For ozone, even with multireference methods, obtaining good convergence globally has proven to be challenging.[57] It remains to be seen whether it will be possible to develop a 6D PES that can fully describe all configurations of O_2 + O + Ar (including placing Ar between O_2 and O) and hence also investigate the chaperone mechanism,[66] or if it will be limited to the region of highly excited O_3 + Ar, relevant to the collisional stabilization of ozone resonances. In some cases, such as demonstrated in a recently reported water–argon PES,[67] a work-around is possible. As long as converged (but not necessarily fully accurate) results can be obtained for distorted geometries using the coupled-cluster method, then one can subtract out separately calculated energies for the isolated distorted fragment, adding back in the energy of the fragment obtained from the most accurate available PES, and hence through this difference, obtain accurate interaction energies. In the case of water–argon, a reported 6D PES[67] is in a sense the best of both worlds, since in the interaction region the non-bonded interactions are described at the coupled-cluster level, but distortions of water are represented by a highly-accurate PES by Polyansky and Tennyson.[68] Unfortunately, this strategy is not applicable to the O_3–Ar sys-

tem since single-reference methods such as coupled-cluster theory fail to converge altogether for large regions of the coordinate space of the distorted ozone molecule (as does DFT). The plan here is to benchmark the non-bonded interactions with ozone at its equilibrium geometry (where the coupled-cluster method is convergent) and then develop a multireference based protocol that matches as closely as possible. The resulting procedure can then be used to construct a flexible 6D PES. The initial steps of constructing a 3D interaction PES using the rigid rotor approximation, where the ozone is kept fixed at its equilibrium position:[57] $r_1 = r_2 = 1.2717$ Å and $\alpha = 116.84°$, are described in this section.

Reference frame and coordinates of the PES

The coordinates used to define the 3D PESs are R, θ and ϕ; where R represents the distance between the center-of-mass of the ozone molecule and the argon atom, while θ and ϕ represent the spherical angles as shown in Figure 1. The origin of the frame of reference is at the center

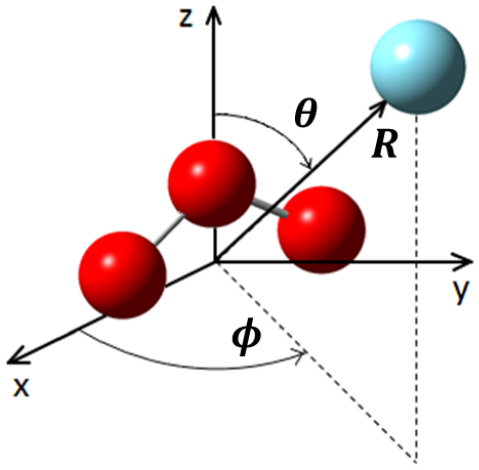

Figure 1: 3D body-fixed coordinate system used to describe the O_3–Ar interaction. The ozone molecule is fixed in the xz plane. The origin of the frame of reference is at the center-of-mass of the ozone molecule, with the z axis along the symmetry axis. The position of the argon atom is defined with respect to the center-of-mass by the spherical coordinates (R, θ, ϕ).

of mass of the ozone molecule. A description of the construction of the PESs in the coordinate range: 2 Å $< R <$ 25 Å, $0 < \theta < \pi$, $0 < \phi < 2\pi$, is given in the following sections.

Ab Initio Calculations

The *ab initio* calculations were performed using two methods and the MOLPRO[69,70] package. The first method is explicitly-correlated CCSD(T)-F12b[71] extended to the complete basis set (CBS) limit. All CBS extrapolations were performed using the simple l^{-3} formula.[72] This approach has been used successfully in numerous studies of spectroscopy and dynamics in van der Waals (vdW) systems,[73–76] and was used here to benchmark the non-bonded interactions. Generally, as reported previously, explicitly-correlated methods are known to converge rapidly with respect to basis set completeness.[77–79] The basis set convergence progression for the well-depth of the complex is given in Table 1. As mentioned above, the coupled-cluster approach fails to converge for significantly distorted geometries of ozone, and thus a multireference based approach was sought. Tests using the MRCI-F12 method[80] and the same VnZ-F12 (n = 2–4) basis set series[81] were conducted along a series of cuts through the PES and compared with the CCSD(T)-F12b/CBS results. Even at the basis set limit, and with inclusion of the Davidson correction, MRCI(Q)-F12/CBS significantly underestimates the O_3–Ar complex stability (see Figure 2). Moreover, calculations performed without symmetry constraints and employing the largest basis set were individually rather time-consuming to consider for the full data set of a global 6D PES. Thus a number of strategies involving scaling the correlation energy (with or without the Davidson correction, or also scaling that contribution) were tested. Ultimately a fortuitously accurate and cost-effective approach was identified. It was discovered that for the various test cuts through the PES, simply scaling the correlation energy (without Davidson correction) using energy contributions obtained using only the smallest VDZ-F12 basis set, could reproduce the benchmark CCSD(T)-F12b/CBS results to within a few wavenumbers. Furthermore, to four significant figures, the best-fit coefficient to achieve the scaling was found to be precisely 1.500.

A complete active space self-consistent field (CASSCF) calculation was used as the reference for the MRCI calculations. O_3–Ar consists of 42 electrons and was treated with 24

Table 1: Basis set convergence test of the potential well-depth of the rigid ozone and argon cluster using the CCSD(T)-F12 method.

Basis	E (cm^{-1})
VDZ-F12	245.22
VTZ-F12	238.56
VQZ-F12	233.25
CBS	229.37

occupied orbitals. For the CASSCF calculations a ($12e$, $9o$) active space was specified, 15 orbitals were closed (the 1s and 2s orbitals of O and 1s, 2s, 3s, 2p and 3p orbitals of Ar were held doubly occupied) while for the MRCI-F12 calculations, only the 8 core orbitals (1s and 2s for O and Ar) were excluded from the correlation treatment. The procedure for obtaining the scaled energy used to construct the MRCI-F12 PES is given in equation (9). It was found that the coupled-cluster CBS limit, $E_{CCSD(T)\text{-}F12b/CBS}$, is well reproduced by scaling the difference between a small-basis MRCI-F12 calculation $E_{MRCI\text{-}F12/VDZ\text{-}F12}$, and the corresponding CASSCF reference $E_{CASSCF/VDZ\text{-}F12}$ (the difference roughly considered as the dynamic correlation energy). The scaling is therefore accounting for the lack of both high-order correlation and basis set completeness.

$$E_{CCSD(T)\text{-}F12b/CBS} \approx E_{CASSCF/VDZ\text{-}F12} + 1.5\,(E_{MRCI\text{-}F12/VDZ\text{-}F12} - E_{CASSCF/VDZ\text{-}F12}) \quad (9)$$

Remarkably, although the scaling factor was determined from only a few test cuts through the PES (Figure 2), as will be seen in the following sections, the complete PES and rovibrational states of the complex are extremely similar for the scaled MRCI-F12/VDZ-F12 and CCSD(T)-F12b/CBS PESs. This is fortuitous and promising for the prospects of constructing an accurate full 6D PES via this approach.

Construction of the PES

After defining the above described schemes for the electronic structure procedures, the two PESs (MRCI-F12 and coupled-cluster based) were constructed using the AUTOSURF

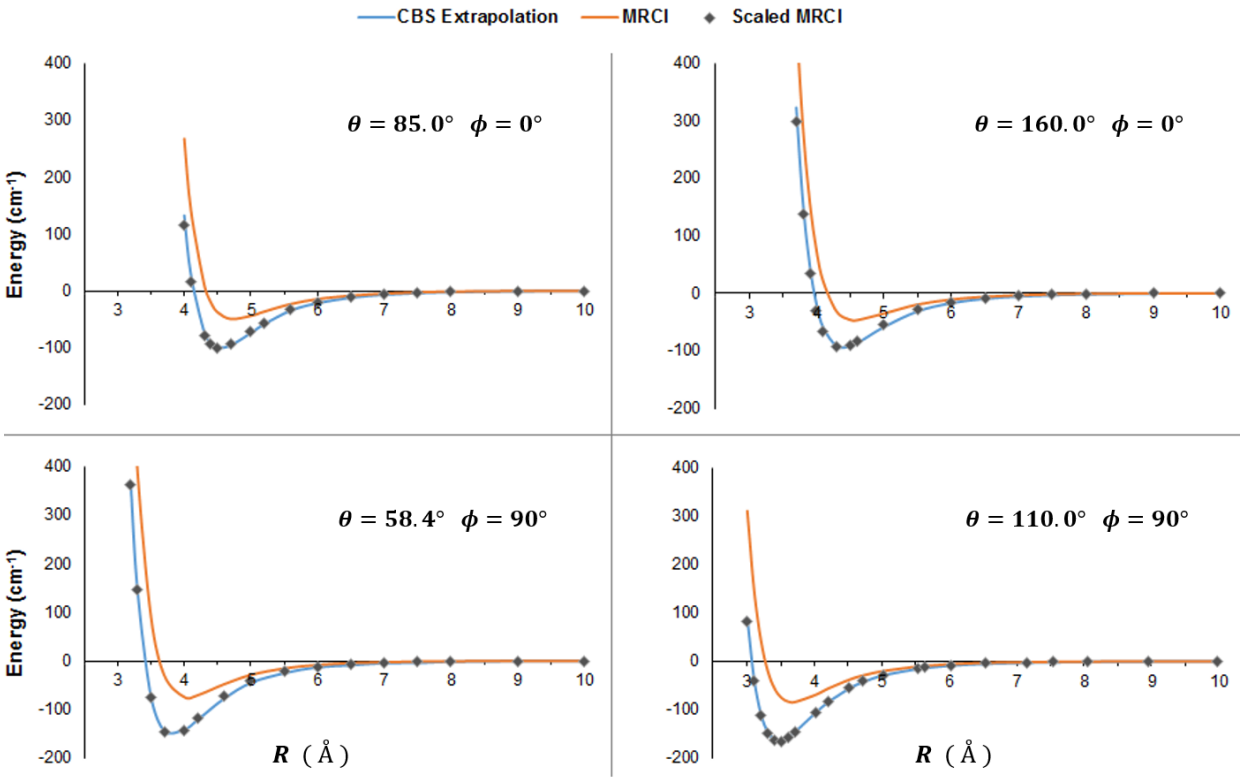

Figure 2: Several 1D cuts through the PES including planar and non-planar geometries. Several angle combinations chosen for determining the MRCI correlation energy scaling factor (see text) are: $\theta = 85°$, $\phi = 0°$; $\theta = 160°$, $\phi = 0°$; $\theta = 58.42°$, $\phi = 90°$; $\theta = 110°$, $\phi = 90°$. The blue line represents CCSD(T)-F12b/CBS energies, while the orange line represents the unscaled MRCI-F12/VDZ-F12 method. Diamond symbols represent the scaled MRCI method and the points are indistinguishable from the CCSD(T)-F12b/CBS results on this scale.

code.[82,83] The scaled MRCI-F12 PES (MRCI-PES) was constructed first using automatically determined data point locations, beginning with a distribution of 1407 *ab initio* energies placed at symmetry unique geometries in the close interaction coordinate range: 2 Å$< R <$ 10 Å, $0 < \theta < \pi$, and $0 < \phi < 2\pi$. The AUTOSURF code uses the L-IMLS method[82–87] of interpolated local expansions to fit these electronic energy data into a PES. Generations of automatically determined points were then added to refine the PES, reaching after several iterations, with 2112 points, a global root mean square (rms) error of 0.632 cm^{-1}. In addition to computing the bound states of the complex reported here, a primary future interest is the study of inelastic collisions of ozone with the argon atom, for which a PES that extends into the long range (*i.e.*, well beyond 10 Å) is required. Hence, a long range continuation of the PES was constructed. To describe the long range, again using the AUTOSURF code, 600 additional *ab initio* points were placed in the slightly overlapping coordinate range: 8 Å$< R <$ 25 Å, $0 < \theta < \pi$, and $0 < \phi < 2\pi$. When required, a smooth transition from the short-range PES to the long-range PES is achieved through a switch using a hyperbolic tangent function centered at 9 Å to connect the two PESs. Thus, using a total of 2712 *ab initio* points, coverage is obtained in the broad coordinate range of 2 Å$< R <$ 25 Å, $0 < \theta < \pi$, and $0 < \phi < 2\pi$.

Similarly, for comparison, a coupled-cluster based PES (CC-PES) at the CCSD(T)-F12b/CBS level was also constructed in the same coordinate range of 2 Å$< R <$ 25 Å, $0 < \theta < \pi$ and $0 < \phi < 2\pi$, beginning with the same data point locations. The topographies of the two PESs turned out to be so similar that no additional automatically generated points were needed to achieve roughly the same estimated fitting error (in this case 0.614 cm^{-1}).

In order to use the PESs to study various isotopologues of ozone, the shift in center-of-mass of the ozone molecule upon isotopic substitution and the associated transformation of the coordinates was determined. This is very straightforward in the 3D case of ozone held rigid at equilibrium, where the intermolecular coordinates can be defined relative to the principal axis frame of each isotopologue. For a flexible 6D PES, making a good choice of the

molecular frame can make dynamics calculations more efficient.[88,89] In our past experience, for small distortions of a water molecule, the Eckart frame has proven effective. There, in a normal mode description of distortions, only the asymmetric stretch rotates the Eckart frame. For the large distortions of ozone, and perhaps even dissociation anticipated in our future studies, it has yet to be determined what the most effective choice of coordinate representation will be.

MCTDH Calculations

The MCTDH method[90,91] is a highly accurate method to solve the time-dependent Schrödinger equation using optimized time-dependent single particle functions (SPF) represented on a time-independent grid—usually a Discrete Variable Representation (DVR)—associated with the different degrees of freedom of the system. The calculations reported here were performed using the freely available Heidelberg MCTDH package.[92] The total wave function expressed as a sum of products of these SPFs can be written as

$$\Psi(Q_1,\cdots,Q_f,t)=\sum_{j_1=1}^{n_1}\cdots\sum_{j_f=1}^{n_f}A_{j_1\cdots j_f}(t)\prod_{\kappa=1}^{f}\phi_{j_\kappa}^{(\kappa)}(Q_\kappa,t)\ , \tag{10}$$

where f is the number of degrees of freedom of the system, $Q_1,\ldots,Q_f$ are the nuclear coordinates, $A_{j_1\cdots j_f}$ are the MCTDH expansion coefficients and $\phi_{j_\kappa}^{(\kappa)}(Q_\kappa,t)$ are the SPFs associated with the κth degree of freedom.

For the MCTDH method to be most efficient, the Hamiltonian operator has to be expressed in a sum-of-products (SOP) form. The kinetic energy operator used for our calculations is the same rigid rotor Hamiltonian used[93] previously in a scattering study of a triatomic molecule–atom vdW system using the MCTDH method. The Hamiltonian is expressed as:

$$\hat{H}=-1/2\mu_R\delta^2/\delta R^2+\hat{\vec{L}}_R^{\dagger}.\hat{\vec{L}}_R/2\mu_R R^2+\hat{T}_{O_3}+\hat{V}_{O_3-Ar}\ , \tag{11}$$

where $\hat{H}$, the Hamiltonian of the triatom–atom system is expressed in the Body-Fixed (BF)

frame. μ_R is the reduced mass of the system and R is the distance between the Ar atom and the center-of-mass of the O_3 molecule. $\hat{\vec{L}}_R$ is the orbital momentum of the system and the product of the orbital momentum with its transpose conjugate can be expanded as:

$$\hat{\vec{L}}_R^{\dagger}.\hat{\vec{L}}_R = \hat{\vec{J}}_{BF}^2 + \hat{\vec{L}}_{O_3,E_2}^2 - 2\hat{J}_{z^{BF}}\hat{L}_{O_3,z^{BF}} - \hat{J}_{-^{BF}}\hat{L}_{O_3,+^{BF}} - \hat{J}_{+^{BF}}\hat{L}_{O_3,-^{BF}} \ , \qquad (12)$$

where E_2 is the frame of reference described by Gatti and Iung.[94] $\hat{V}_{O_3-Ar}$ is the intermolecular PES presented in the previous section, while $\hat{T}_{O_3}$ is the Kinetic Energy Operator (KEO) of the molecule.

The KEO for the ozone molecule, when expressed in polyspherical coordinates—as it is here—is already in a SOP form and can be expressed as:[93]

$$\hat{T}_{O_3} = \big((A+C)/2\big)\hat{\vec{L}}_{O_3,BF}^2 + \Big[B - \big((A+C)/2\big)\Big]\hat{\vec{L}}_{O_3,z^{BF}}^2 + \big((A-C)/4\big)\Big[\hat{\vec{L}}_{O_3,+^{BF}}^2 + \hat{\vec{L}}_{O_3,-^{BF}}^2\Big]. \quad (13)$$

The frame of reference in this case, has the origin fixed at the center-of-mass of the ozone molecule, with the z axis passing through the argon atom. The angles α_{O_3}, β_{O_3} and γ_{O_3} are the set of new transformed Euler angles in this frame of reference. The spherical angles, θ and ϕ used for constructing the PESs become β_{O_3} and γ_{O_3} respectively. The Hamiltonian, in this case, is represented in Jacobi coordinates. The rotational constants A, B and C used for the $^{48}O_3$–Ar system are 3.55366659 cm^{-1}, 0.44528320 cm^{-1} and 0.39475182 cm^{-1} respectively,[95] while the reduced mass (μ) used is 21.80383583 amu. The fitted PESs described above are not straightforwardly in the SOP form and therefore were re-expressed. For low dimensional problems (up to 6D), the `potfit` algorithm[96,97] implemented in the MCTDH package can define an accurate SOP representation efficiently, and was employed here. Calculations of the rovibrational states were done using the block improved relaxation method.[98–100] The improved relaxation method is an MCSCF-type approach to solve the time independent Schrödinger equation. The SPFs associated with the degrees of freedom are optimized by relaxation (*i.e.,* propagation in imaginary time). The Hamiltonian matrix is then evaluated

Table 2: Parameters of the primitive basis for the $J = 0$ calculations. FFT stands for Fast Fourier Transform, Wigner for Wigner-DVR, and Exp for Exponential-DVR. K is the momentum representation of the first Euler angle. The distance is in bohr and the angles are in radian.

	R	β_{O_3}	γ_{O_3}	α_{O_3}
Primitive basis	FFT	Wigner	Exp	K
Number of points	256	37	73	1
Range	3.0–23.0	$0-\pi$	$0-2\pi$	0
Size of SPF basis	50		160	

from the set of current SPFs. The coefficient vector (A) represented in equation (10), is then obtained from the diagonalization of the Hamiltonian matrix. In the block improved relaxation method, the propagation of a block of initial vectors converge together to a set of eigenstates. Hence, this method efficiently obtains several eigenstates simultaneously.

As shown in Table 2, the parameters for the calculations were selected as follows: for the radial coordinate, 256 sine DVR points were placed in the range of $R = [3, 23]$ bohr, while for the angle β_{O_3} 37 Wigner DVR functions[101,102] were used in the [0, π] range; 73 exponential DVR points were used in the [0, 2π] range for γ_{O_3}. For the $J = 0$ rovibrational calculations, 50 and 160 SPFs were used for the radial (R) and angular parts respectively, with 8 packets for the propagation, while 50 and 200 were used for the radial and angular parts respectively for the $J = 1$–6 calculations. The angular part consists of β_{O_3}, γ_{O_3}, and α_{O_3} (where α_{O_3} is the momentum representation for a particular state—*i.e.*, for $J = 0$ calculations, K is 0, while for $J = 1$ calculations, K is -1, 0, 1). K goes from $-J$ to $+J$ for the calculations of higher J.

For the 686 and 668 O_3–Ar calculations, aside from the coordinate transformed PES, all of the parameters are the same except for the rotational constants and reduced mass. For the 686 O_3–Ar calculations, the rotational constants used are:[95] $A = 3.29049897$ cm^{-1}, $B = 0.44539922$ cm^{-1}, and $C = 0.39132965$ cm^{-1} while for the 668 O_3–Ar system, the rotational constants used are:[95] $A = 3.48818517$ cm^{-1}, $B = 0.42000833$cm^{-1}, and $C = 0.37400895$ cm^{-1}. The reduced mass (μ) for the 686 and 668 O_3–Ar systems is 22.20843419 amu.

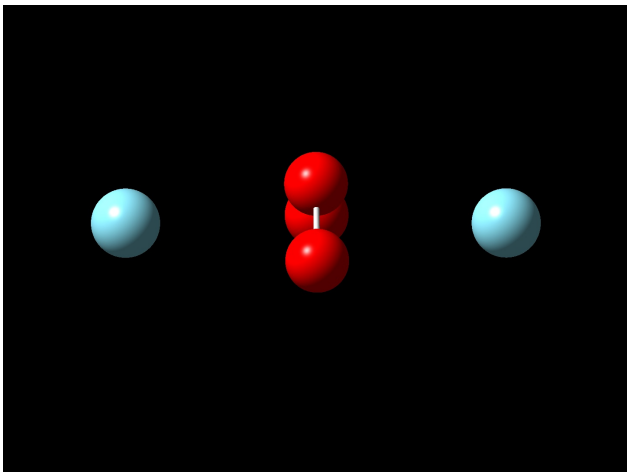

Figure 3: Illustration of the symmetry-equivalent wells located on opposite faces of the ozone molecule.

Results and Discussion

The PES for O_3–Ar is characterized by two symmetry-equivalent wells (one on each opposite face of the ozone molecule) with a benchmark depth of 229.4 cm^{-1} at the CCSD(T)-F12b/CBS level. This is illustrated in Figure 3, where the argon atom is shown in both wells simultaneously (in fact, the rovibrational wavefunctions do delocalize into the two wells). For the 666 and 686 O_3–Ar complexes, there are two vertical reflection planes of symmetry (one passing through the three O-atoms, and a second plane perpendicular to the first, passing through the two wells, or Ar-atom positions in Figure 3), while for the 668 O_3–Ar complex, due to the skewed shift of the center-of-mass point for the ozone fragment, only the symmetry plane passing through the oxygen nuclei is preserved.

Contour plots for the fitted CCSD(T)-F12b/CBS and scaled MRCI-F12 PESs are shown in Figure 4. Each plot represents the full range of the two angle coordinates and for each angle-pair point on the plot, the energy with respect to the radial coordinate R has been relaxed. As mentioned above, it was found to be possible to achieve remarkably close agreement between the benchmark CCSD(T)-F12b/CBS energies and those obtained by simple scaling of the correlation energy in MRCI-F12/VDZ-F12 calculations. Indeed, the well-depths of the fitted PESs are nearly identical (229.64 cm^{-1} and 229.70 cm^{-1} for the coupled-cluster

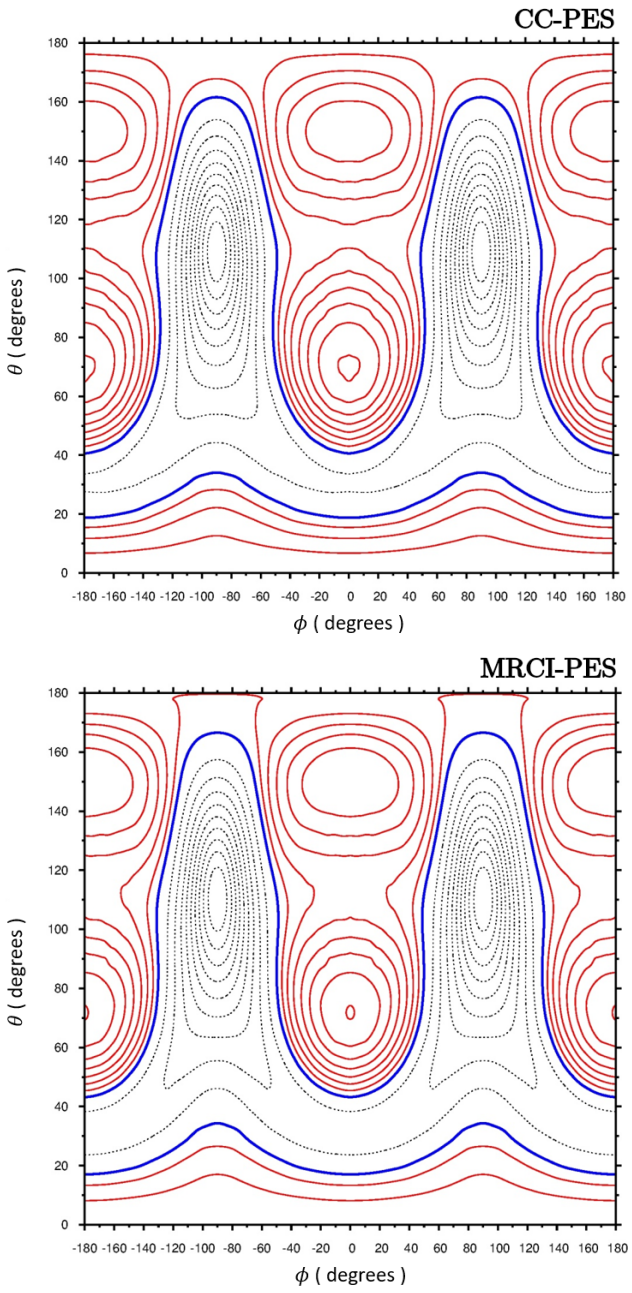

Figure 4: R-optimized plots of the fitted CC-PES (top) and MRCI-PES (bottom). For each pair of angles the energy is optimized with respect to the center-of-mass distance R. The blue line represents the energy $E_0 = -130$ cm^{-1}. Dashed (solid) contours represent energies below (above) E_0, in 10 cm^{-1} (5 cm^{-1}) intervals.

and MRCI based PESs respectively). The rms deviation between the two PESs—evaluated over the entire grid of 16 471 points plotted in Figure 4—is only 2.72 cm^{-1}. The equilibrium intermolecular structural parameters, very similar for the two PESs, are given in Table 3.

Table 3: Geometric parameters—and energy—for each critical point of the CC and MRCI O_3–Ar PES. V_{min} represents the energy at the bottom of the well. $V_{barrier}$ represents the energy of the barrier—at the transition structure (TS)—between the two equivalent wells. ZPE refers to the zero-point energy. All distances are in Angströms, angles in degrees, and energies in wave numbers.

	CC-PES	MRCI-PES
R_{min}	3.299	3.295
θ_{min}	109.90	110.15
ϕ_{min}	90.00	90.00
V_{min}	-229.64	-229.70
R_{TS}	3.299	3.295
θ_{TS}	30.21	31.95
ϕ_{TS}	0.00	0.00
$V_{barrier}$	-141.58 (88.06*)	-146.77 (82.93*)
ZPE	-162.69 (66.95*)	-163.66 (66.04*)

* Energy with respect to the global minima of the PES.

Perhaps the most significant difference between the two PESs is the height of the barrier along the relaxed path between the two minima. For the CC-PES, the height of the barrier between the wells (energy: -141.58 cm^{-1}) is 88.06 cm^{-1}, while for the MRCI-PES, it is slightly less: 82.93 cm^{-1}. As expected, this difference in barrier heights does affect the tunneling splittings recorded in the rovibrational calculations of the complex.

Using the parameters given in Table 2 and in the provided *Supporting Information* (SI)—*cf.* Table S2, rovibrational calculations up to $J = 6$ were performed using the block improved relaxation method in the MCTDH code package. The zero point energy was computed as 66.95 cm^{-1} and 66.04 cm^{-1} using the CC- and MRCI-based PESs respectively (Tables 3 and 4). The low-lying $J = 0$ vibrational states occur in even/odd parity pairs with small tunneling splittings. The splitting for the lowest pair of states on the MRCI-based PES is slightly larger (0.021 cm^{-1}) than for the CC-based PES (0.014 cm^{-1}) due to the slightly lower barrier. Only the first even/odd pair of levels is energetically below the barrier between wells. The next few higher levels do come in even/odd pairs, but delocalize significantly since they are above the barrier. The splittings become larger and eventually the pairs of states interpenetrate each other and lose clearly assignable modal character. Nevertheless, the

Table 4: Vibrational levels for $J = 0$ for the first 20 states. ΔEnergy represents the energy gap of the levels from the ZPE for the two PESs of $^{48}O_3$–Ar.

	CC-PES		MRCI-PES	
ν_1 ν_2 ν_3	Energy (cm^{-1})	ΔEnergy (cm^{-1})	Energy (cm^{-1})	ΔEnergy (cm^{-1})
000	-162.690	0.000	-163.662	0.000
000	-162.675	0.014	-163.641	0.021
001	-134.419	28.271	-135.621	28.041
001	-134.375	28.315	-135.564	28.098
100	-131.582	31.107	-132.373	31.288
100	-131.427	31.263	-132.199	31.462
010	-123.856	38.834	-125.142	38.520
010	-122.962	39.728	-124.053	39.609
101	-115.945	46.745	-118.600	45.062
011	-114.632	48.057	-117.329	46.332
101	-113.331	49.359	-115.334	48.327
002	-112.441	50.249	-114.262	49.400
011	-109.460	53.229	-111.101	52.561
111	-107.486	55.204	-108.821	54.841
002	-105.197	57.492	-106.567	57.095
111	-104.446	58.244	-105.137	58.525
200	-103.534	59.155	-104.522	59.140
012	-102.557	60.133	-104.422	59.240
102	-100.882	61.807	-101.698	61.964
012	-100.357	62.333	-100.449	63.213

vibrational levels computed for the two PESs are remarkably similar, agreeing to within 1 cm^{-1} for all the levels given in Table 4. This confirms the fortuitously close match of the scaled MRCI method to that of the benchmark CC approach. Table 4 provides a comparison of the energies and modal assignments for the first 20 vibrational levels of the two PESs.

The modal character for each vibrational level given in Table 4 was assigned by visual inspection of probability density plots for each state. The quantum numbers ν_1, ν_2, and ν_3, listed in the first column of Table 4, represent the number of nodes in the R, θ, and ϕ coordinates respectively. The first few states (shown in Figure 5) are straightforward to assign this way, but the assignment becomes more complicated for higher lying states (as can be seen in Figure 6).

Rovibrational levels for $J = 1$–6 were also calculated, and in that range of J, the vibra-

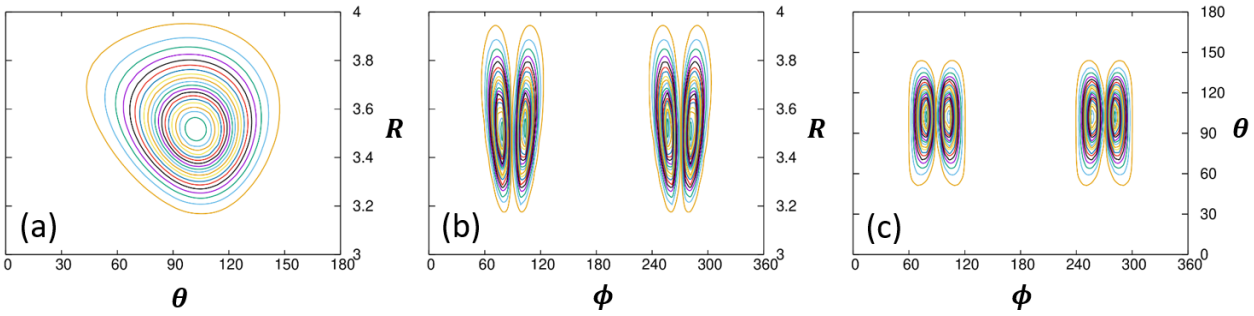

Figure 5: Probability density plots of the lowest (even) 001 state. All distances are in Angströms, angles in degrees.

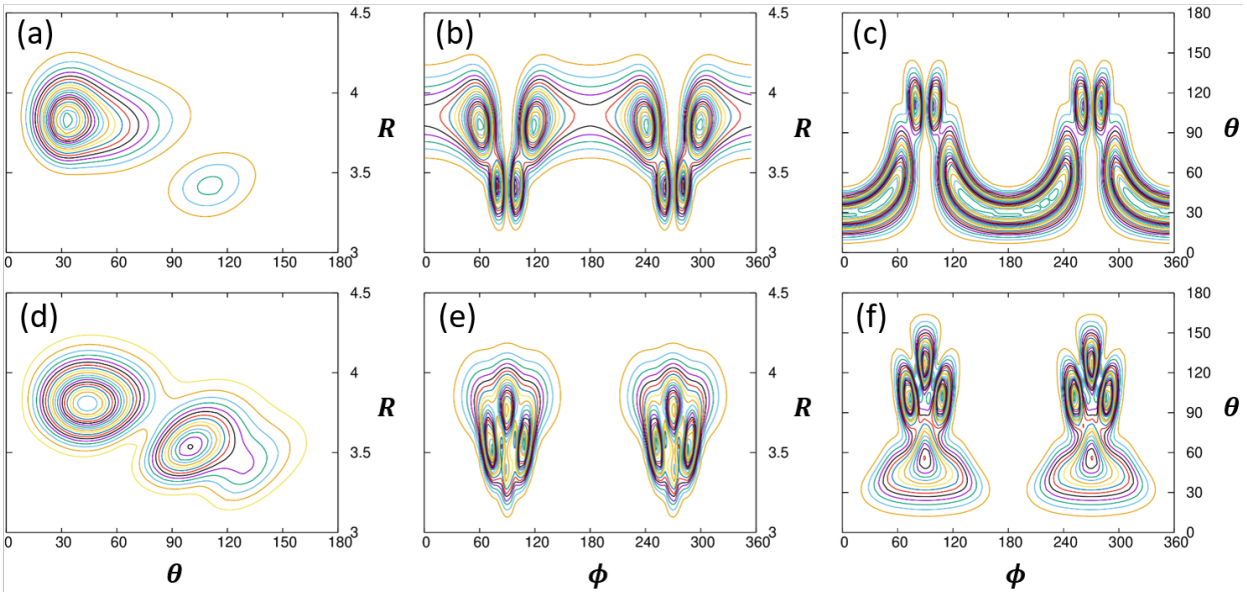

Figure 6: Probability density plots of wave functions of mixed states: 101 (a)–(c) and 002 (d)–(f). All distances are in Angströms, angles in degrees.

tional parents were found to be very similar to those of the $J = 0$ calculations. Due to the two equivalent wells, and the resulting even/odd parity pairs for each vibrational state, then prior to considerations of nuclear spin statistics, a doubling of computed rovibrational levels was recorded. For example, corresponding to the lowest, nodeless vibrational state, 6 levels were recorded for $J = 1$, and 10 vibrational levels for $J = 2$. These are simply the expected $2J + 1$ rotational components, but with a separate set associated with each of the even and odd parity vibrational parents. The computed splitting between each particular rotational component associated with one particular vibrational parent, and the corresponding state

with the same rotational component, associated with the even/odd vibrational partner, was found to be nearly identical within each group of states, and in fact in this range of J, almost exactly that of the $J = 0$ tunneling splittings. For $^{48}O_3$, the tunneling splitting is not directly observable since due to the nuclear spin statistical requirements for "identical bosons," only total wavefunctions that are symmetric upon O-atom exchange are allowed. The result is that for $^{48}O_3$ (or the symmetric 686 isotopologue), only the usual $2J + 1$ states exist. However, which particular states are shown to exist (via symmetry analysis), has fascinating implications for the interpretation of the relationship between rovibrational transition frequencies and the structure of the complex. It turns out, as will be detailed next, that the allowed states are distributed across both even/odd parity vibrational parents, and therefore the rovibrational transitions recorded between those states include also the tunneling splitting gap, and hence lose their usual precise relation to structure and moments of inertia. We consider the symmetry of the complex for 666 and 686 isotopologues using the G_4 group. The irreducible representations (irreps) of this group are A^+, A^-, B^+ and B^-. For the total wave function to be symmetric upon feasible O-atom exchange, it must be either A^+ or A^- symmetry. The total wave function is a product of the electronic, rotational, vibrational and nuclear spin wave functions, and here the electronic and nuclear spin wave functions are of A^+ symmetry. This means that the product of the symmetries of the vibrational parent and rotational components determine whether the state is allowed. Collecting the relevant data from the *Molecular Spectroscopy* book by Bunker and Jensen[103] (see Table 5), the symmetry for the rotational wavefunction component is determined based on the K_a and K_c projections. The rotational wave function can combine with either an odd parity or even parity vibrational level to be an allowed state. The vibrational contribution is A^+ for even parity parents, and B^- for odd. Allowed rotational transitions involve a switch in parity and hence many of the recorded transitions go from one type of even/odd parent to another (depending also on the symmetry of the rotational component). For example, the 0_{00} - 1_{10} transition given in Table 6 goes from the lower, even vibrational parent to the upper, odd

Table 5: G_4 molecular symmetry group table for the rotational wave function (o = odd, e = even).

G_4	E	(12)	E^*	$(12)^*$	$\mid K_a K_c >$
A^+	1	1	1	1	e e
A^-	1	1	-1	-1	e o
B^-	1	-1	-1	1	o o
B^+	1	-1	1	-1	o e

vibrational parent and hence that frequency is partly due to the tunneling splitting between the even and odd vibrational parents. This is also the case for the 1_{01} - 1_{11} transition, but is not true for the 1_{11} - 1_{10} transition which is between states that share a vibrational parent. In general, whether or not a given transition is between different vibrational parents and hence includes a tunneling splitting contribution depends on the symmetries of the rotational state components given in Table 5 and the corresponding vibrational parent required to make an allowed state. The remarkable implication of this is that many of the observed rotational transition frequencies have imbedded in them the energy of the tunneling splitting between the even/odd vibrational parents, and is not simply related to moments of inertia and structure. This means that the structure of the complex can't be directly inferred from the rotational spectrum. Indeed, while the contribution of the tunneling splitting is fairly small for the lowest vibrational states, it becomes much larger for higher states and would lead to absurd naive interpretations of the structure.

In 1979, DeLeon *et al.*[104] studied the microwave spectrum of $^{48}O_3$–Ar, reporting transition frequencies, and deriving rotational constants and structural parameters of the complex (without consideration of the implications of the two wells and tunneling splitting). Their measurements are used to benchmark the calculated values in this study. In our calculations, transition frequencies were obtained from energy differences between the allowed states as determined from the rovibrational calculations and symmetry analysis. The calculated transitions are very close to the experimental ones (see Table 6), validating the accuracy of the PESs. Although results for the two PESs are very similar, the CC-based PES produced calculated transitions in slightly better agreement with experiment than those of the MRCI

PES. The rms deviation for the series of transitions reported by DeLeon *et al.*, computed using the CC-based PES is 0.001 cm^{-1}, while the corresponding value for the MRCI-based PES is 0.004 cm^{-1}. Note that since the tunneling splitting contributes to the transition frequencies, the level of agreement with experiment can be viewed as partly related to the different barrier heights between wells in addition to the topography of the PESs deep in the wells themselves. Overall, the results are viewed as remarkably good for both methods and confirmation that the derived levels of electronic structure theory provide a realistic description of this system. Of course it is possible that unanticipated difficulties will be encountered during construction of a 6D PES.

Table 6: Comparison of observed and calculated transition frequencies(MHz).

	Experimental[104]	Calculated	
		CC-PES	MRCI-PES
0_{00} - 1_{10}	14632.849	14593.516	14810.466
1_{01} - 1_{11}	10738.910	10723.942	10923.181
1_{11} - 1_{10}	231.435	228.897	231.015
1_{10} - 2_{02}	3649.648	3675.739	3844.259
2_{11} - 3_{12}	11329.240	11263.804	11307.305
2_{02} - 3_{03}	10970.282	10911.192	10949.811
2_{11} - 3_{03}	234.635	273.578	439.276
2_{12} - 2_{11}	694.196	686.576	693.293
3_{13} - 3_{12}	1387.972	1369.267	1385.487
4_{14} - 4_{13}	2312.464	2286.993	2308.229
5_{15} - 5_{14}	3466.672	3428.408	3460.293
2_{21} - 2_{20}	3.846	3.753	3.089
3_{22} - 3_{21}	19.215	18.68	19.122
4_{04} - 4_{14}	9748	9739	9929
5_{05} - 5_{15}	9229	9225	9411
4_{23} - 4_{22}	57	56	57
5_{24} - 5_{23}	134	131	133
6_{25} - 6_{24}	267	261	266

Since they were reported by DeLeon *et al.*,[104] we also computed asymmetric top rotational constants in the same manner, using the transition frequencies (see Table 7). Note however the above discussion about the impact of the tunneling splitting on the transition frequencies and hence the lack of direct geometric interpretations of any derived rotational constants.

Table 7: Comparison of the calculated and experimental Rotational Constants (all values are in MHz).

	Experimental[104]	Calculated	
		CC-PES	MRCI-PES
A	12686	12659	12867
B	1947	1935	1944
C	1716	1706	1713

Nevertheless, the impact of this on the lowest state was found to be small. The expectation values of the center-of-mass coordinate R for the lowest rovibrational state computed on the scaled MRCI- and CC-based PESs are 3.44 Å and 3.45 Å respectively, compared with the corresponding structural parameter derived by DeLeon *et al.* of 3.42 Å.

The effect of isotopic substitution on the rovibrational states of the complex was also studied. Studies of the 686 and 668 isotopologues were performed using the same PESs, simply by applying the appropriate transformations of coordinates. The geometric parameters, and energy, for each critical point of all considered isotopologues of ozone (MRCI O_3–Ar PESs), are given as *Supporting Information—cf.* Table S1. Compared to the parent system, the 686 ozone molecule has slightly different rotational constants and a larger total mass, but follows the same symmetry considerations as described above for the 666 complex, and thus the same pattern of allowed states and transitions. For the 668 O_3–Ar complex, one vertical plane of symmetry is lost, and the coordinate transformation skews the PES such that the path between wells is different around the two different ends of the 668 ozone molecule. This can be appreciated in Figure S2 of the SI, where the angle θ along the lowest energy path near $\phi = -180°$, or 180°, is seen to be significantly different than at $\phi = 0°$. Due to breaking the symmetry (the two end-O-atoms are distinguishable), the symmetry number of 668 O_3 is reduced to one, and all of the computed states of the complex are allowed. Considering also the slight increase in system mass, this amounts to slightly more than doubling the density of states.

The levels for the 686 and 668 O_3–Ar complexes were also computed using the MCTDH approach and the same parameters (see Table 2). The results are given in Tables S3 and S4

(in the SI) up to $J = 6$. Corresponding experimental measurements have not been reported for these isotopologues, but it is safe to assume that accuracy of the calculated levels is similar to those of the parent 666 O_3–Ar complex.

Conclusion

The states and dynamics of O_3–M systems are relevant to understanding the collisional stabilization step in the formation of ozone in the atmosphere. Anomalous populations of heavy isotopologues of ozone in the atmosphere are believed to arise from this step in the overall cycle of formation and destruction. Here, for M, argon was chosen as the most convenient monatomic collision partner. Ultimately, in order to simulate stabilizing collisions with highly excited rovibrational resonance states of ozone (neglecting non-adiabatic effects), a single fully flexible 6D PES is required. In this paper, as an initial step, we benchmark the O_3–Ar complex stability with O_3 held at its equilibrium geometry. A well-depth for the complex of 229.4 cm^{-1} was determined at the CCSD(T)-F12b/CBS level and a 3D PES—describing ozone as a rigid rotor interacting with the argon atom—was constructed at this level of electronic structure theory. The electronic structure of ozone is complex and significant distortions of the molecule require a multireference description. Thus, as a necessary development—looking ahead to the construction of a flexible 6D PES—a multireference MRCI-F12 based protocol was developed that closely matches the behavior of the CCSD(T)-F12b/CBS benchmark. Using these two PESs, vibrational bound-state calculations were performed for $J = 0$, and for the lowest vibrational parent state rovibrational states were computed up to $J = 6$. A symmetry analysis was performed to determine the allowed states for the 666, 686, and 668 isotopologues. For the parent $^{48}O_3$–Ar complex, computed transition energies between symmetry-allowed states were compared with previously reported results of microwave experiments. Remarkably close agreement with the experimental transitional frequencies and rotational constants was obtained, which is an im-

portant validation of the accuracy of the PESs and underlying levels of electronic structure theory. The effect of isotopic substitution on this system was also studied. As expected, moving from 666 to 686 O_3–Ar the density of states increases only slightly due the mass increase. However, for 668 O_3–Ar the reduced symmetry results in roughly a further doubling of the density of states. A forthcoming paper explores the impact of the state densities on the rates of collisional energy transfer and hence the formation rates for various isotopologues of ozone.

Acknowledgements

The authors acknowledge helpful discussions with Professor Nasser Moazzen-Ahmadi (Calgary). This work was supported by the US National Science Foundation (No. CHE-1566246).

References

(1) Chapman, S. A theory of upperatmospheric ozone. *Mem. Roy. Meteor.* **1930**, *3*, 103–125.

(2) Kaiser, J.; Röckmann, T.; Brenninkmeijer, C. A. Contribution of mass-dependent fractionation to the oxygen isotope anomaly of atmospheric nitrous oxide. *J. Geophys. Res.:Atmos.* **2004**, *109*, D03305.

(3) Solomon, S. Stratospheric ozone depletion: A review of concepts and history. *Rev. Geophys.* **1999**, *37*, 275–316.

(4) Yung, Y. L.; Lee, A. Y.; Irion, F. W.; DeMore, W. B.; Wen, J. Carbon dioxide in the atmosphere: Isotopic exchange with ozone and its use as a tracer in the middle atmosphere. *J. Geophys. Res.:Atmos.* **1997**, *102*, 10857–10866.

(5) Chakraborty, S.; Bhattacharya, S. Experimental investigation of oxygen isotope exchange between CO_2 and $O(^1D)$ and its relevance to the stratosphere. *J. Geophys. Res.:Atmos.* **2003**, *108*.

(6) Mauersberger, K. Measurement of heavy ozone in the stratosphere. *Geophys. Res. Lett.* **1981**, *8*, 935–937.

(7) Mauersberger, K. Ozone isotope measurements in the stratosphere. *Geophys. Res. Lett.* **1987**, *14*, 80–83.

(8) Thiemens, M. H.; Heidenreich, J. E. The mass-independent fractionation of oxygen: A novel isotope effect and its possible cosmochemical implications. *Science* **1983**, *219*, 1073–1075.

(9) Thiemens, M. H. Mass-independent isotope effects in planetary atmospheres and the early solar system. *Science* **1999**, *283*, 341–345.

(10) Mauersberger, K.; Erbacher, B.; Krankowsky, D.; Günther, J.; Nickel, R. Ozone isotope enrichment: Isotopomer-specific rate coefficients. *Science* **1999**, *283*, 370–372.

(11) Morton, J.; Barnes, J.; Schueler, B.; Mauersberger, K. Laboratory studies of heavy ozone. *J. Geophys. Res.:Atmos.* **1990**, *95*, 901–907.

(12) Anderson, S.; Hülsebusch, D.; Mauersberger, K. Surprising rate coefficients for four isotopic variants of $O+O_2+M$. *J. Chem. Phys.* **1997**, *107*, 5385–5392.

(13) Janssen, C.; Guenther, J.; Krankowsky, D.; Mauersberger, K. Relative formation rates of $^{50}O_3$ and $^{52}O_3$ in ^{16}O–^{18}O mixtures. *J. Chem. Phys.* **1999**, *111*, 7179–7182.

(14) Janssen, C.; Guenther, J.; Krankowsky, D.; Mauersberger, K. Erratum: "Relative formation rates of $^{50}O_3$ and $^{52}O_3$ in ^{16}O–^{18}O mixtures" [J. Chem. Phys. 111, 7179 (1999)]. *J. Chem. Phys.* **2000**, *112*, 11109–11109.

(15) Wolf, S.; Bitter, M.; Krankowsky, D.; Mauersberger, K. Multi-isotope study of fractionation effects in the ozone formation process. *J. Chem. Phys.* **2000**, *113*, 2684–2686.

(16) Ndengué, S.; Madronich, S.; Gatti, F.; Meyer, H.-D.; Motapon, O.; Jost, R. Ozone photolysis: Strong isotopologue/isotopomer selectivity in the stratosphere. *J. Geophys. Res.:Atmos.* **2014**, *119*, 4286–4302.

(17) Cole, A. S.; Boering, K. A. Mass-dependent and non-mass-dependent isotope effects in ozone photolysis: Resolving theory and experiments. *J. Chem. Phys.* **2006**, *125*, 184301.

(18) Haverd, V.; Toon, G. C.; Griffith, D. W. Evidence for altitude-dependent photolysis-induced 18O isotopic fractionation in stratospheric ozone. *Geophys. Res. Lett.* **2005**, *32*.

(19) Krankowsky, D.; Lämmerzahl, P.; Mauersberger, K.; Janssen, C.; Tuzson, B.; Röckmann, T. Stratospheric ozone isotope fractionations derived from collected samples. *J. Geophys. Res.:Atmos.* **2007**, *112*.

(20) Liang, M.-C.; Irion, F. W.; Weibel, J. D.; Miller, C. E.; Blake, G. A.; Yung, Y. L. Isotopic composition of stratospheric ozone. *J. Geophys. Res.:Atmos.* **2006**, *111*.

(21) Sato, T.; Kuribayashi, K.; Yoshida, N.; Kasai, Y. Diurnal variation of oxygen isotopic enrichment in asymmetric-18 ozone observed by the SMILES from space. *Geophys. Res. Lett.* **2017**, *44*, 6399–6406.

(22) Chakraborty, S.; Bhattacharya, S. Oxygen isotopic fractionation during UV and visible light photodissociation of ozone. *J. Chem. Phys.* **2003**, *118*, 2164–2172.

(23) Heidenreich III, J. E.; Thiemens, M. H. A non-mass-dependent oxygen isotope effect in the production of ozone from molecular oxygen: The role of molecular symmetry in isotope chemistry. *J. Chem. Phys.* **1986**, *84*, 2129–2136.

(24) Guenther, J.; Krankowsky, D.; Mauersberger, K. Third-body dependence of rate coefficients for ozone formation in ^{16}O–^{18}O mixtures. *Chem. Phys. Lett.* **2000**, *324*, 31–36.

(25) Jasper, A. W.; Oana, C. M.; Miller, J. A. Third-body collision efficiencies for combustion modeling: Hydrocarbons in atomic and diatomic baths. *Proc. Combust. Inst.* **2015**, *35*, 197–204.

(26) Quack, M. Detailed symmetry selection rules for reactive collisions. *Mol. Phys.* **1977**, *34*, 477–504.

(27) Mauersberger, K.; Lämmerzahl, P.; Krankowsky, D. Stratospheric ozone isotope enrichments–revisited. *Geophys. Res. Lett.* **2001**, *28*, 3155–3158.

(28) Babikov, D.; Kendrick, B. K.; Walker, R. B.; T Pack, R.; Fleurat-Lesard, P.; Schinke, R. Metastable states of ozone calculated on an accurate potential energy surface. *J. Chem. Phys.* **2003**, *118*, 6298–6308.

(29) Babikov, D.; Kendrick, B.; Walker, R.; Schinke, R.; Pack, R. Quantum origin of an anomalous isotope effect in ozone formation. *Chem. Phys. Lett.* **2003**, *372*, 686–691.

(30) Babikov, D.; Kendrick, B. K.; Walker, R. B.; T Pack, R.; Fleurat-Lesard, P.; Schinke, R. Formation of ozone: Metastable states and anomalous isotope effect. *J. Chem. Phys.* **2003**, *119*, 2577–2589.

(31) Teplukhin, A.; Babikov, D. Several levels of theory for description of isotope effects in ozone: Symmetry effect and Mass effect. *J. Phys. Chem. A* **2018**, *122*, 9177–9190.

(32) Gao, Y. Q.; Marcus, R. Strange and unconventional isotope effects in ozone formation. *Science* **2001**, *293*, 259–263.

(33) Gao, Y. Q.; Marcus, R. On the theory of the strange and unconventional isotopic effects in ozone formation. *J. Chem. Phys.* **2002**, *116*, 137–154.

(34) Gao, Y. Q.; Chen, W.-C.; Marcus, R. A theoretical study of ozone isotopic effects using a modified ab initio potential energy surface. *J. Chem. Phys.* **2002**, *117*, 1536–1543.

(35) Hathorn, B.; Marcus, R. An intramolecular theory of the mass-independent isotope effect for ozone. II. Numerical implementation at low pressures using a loose transition state. *J. Chem. Phys.* **2000**, *113*, 9497–9509.

(36) Jasper, A. W.; Pelzer, K. M.; Miller, J. A.; Kamarchik, E.; Harding, L. B.; Klippenstein, S. J. Predictive a priori pressure-dependent kinetics. *Science* **2014**, *346*, 1212–1215.

(37) Alexander, M. H.; Jendrek, E. F.; Dagdigian, P. J. Validity of energy gap representations of rotationally inelastic cross sections between polar molecules. *J. Chem. Phys.* **1980**, *73*, 3797–3803.

(38) Alexander, M. H.; Hall, G. E.; Dagdigian, P. J. The approach to equilibrium: Detailed balance and the master equation. *J. Chem. Educ.* **2011**, *88*, 1538–1543.

(39) Chakraborty, S.; Bhattacharya, S. Oxygen isotopic anomaly in surface induced ozone dissociation. *Chem. Phys. Lett.* **2003**, *369*, 662–667.

(40) Bhattacharya, S.; Chakraborty, S.; Savarino, J.; Thiemens, M. H. Low-pressure dependency of the isotopic enrichment in ozone: Stratospheric implications. *Geophys. Res.: Atmos.* **2002**, *107*, 4675.

(41) Sun, Z.; Yu, D.; Xie, W.; Hou, J.; Dawes, R.; Guo, H. Kinetic isotope effect of the $^{16}O+^{36}O_2$ and $^{18}O+^{32}O_2$ isotope exchange reactions: Dominant role of reactive resonances revealed by an accurate time-dependent quantum wavepacket study. *J. Chem. Phys.* **2015**, *142*, 174312.

(42) Lahankar, S. A.; Zhang, J.; Minton, T. K.; Guo, H.; Lendvay, G. Dynamics of the

O-Atom Exchange Reaction $^{16}O(^3P) + {}^{18}O{}^{18}O(^3\Sigma_g^-) \rightarrow {}^{16}O{}^{18}O(^3\Sigma_g^-) + {}^{18}O(^3P)$ at Hyperthermal Energies. *J. Phys. Chem. A* **2016**, *120*, 5348–5359.

(43) Gelb, A. Classical trajectory study of energy transfer between argon atoms and vibrationally-rotationally excited ozone molecules. *J. Phys. Chem.* **1985**, *89*, 4189–4194.

(44) Stace, A. J.; Murrell, J. N. Dynamics of the oxygen exchange reaction. *J. Chem. Soc., Faraday Trans. 2* **1978**, *74*, 2182–2186.

(45) Gross, A.; Billing, G. D. Rate constants for ozone formation. *Chem. Phys.* **1994**, *187*, 329–335.

(46) Gross, A.; Billing, G. D. Rate constants for ozone formation and for isotopic exchange reactions. *Chem. Phys.* **1993**, *173*, 393–406.

(47) Gross, A.; Billing, G. D. Isotope effects on the rate constants for the processes $O_2 + O \rightarrow O + O_2$ and $O_2 + O + Ar \rightarrow O_3 + Ar$ on a modified ground-state potential energy surface for ozone. *Chem. Phys.* **1997**, *217*, 1–18.

(48) Charlo, D.; Clary, D. C. Quantum-mechanical calculations on termolecular association reactions XY + Z + M → XYZ + M: application to ozone formation. *J. Chem. Phys.* **2002**, *117*, 1660–1672.

(49) Charlo, D.; Clary, D. C. Quantum-mechanical calculations on pressure and temperature dependence of three-body recombination reactions: Application to ozone formation rates. *J. Chem. Phys.* **2004**, *120*, 2700–2707.

(50) Ivanov, M.; Schinke, R. Vibrational energy transfer in Ar–O_3 collisions: comparison of rotational sudden, breathing sphere, and classical calculations. *Mol. Phys.* **2010**, *108*, 259–268.

(51) Xie, T.; Bowman, J. M. Quantum inelastic scattering study of isotope effects in ozone stabilization dynamics. *Chem. Phys. Lett.* **2005**, *412*, 131–134.

(52) Ivanov, M. V.; Babikov, D. Mixed quantum-classical theory for the collisional energy transfer and the rovibrational energy flow: Application to ozone stabilization. *J. Chem. Phys.* **2011**, *134*, 144107.

(53) Ivanov, M. V.; Babikov, D. Collisional stabilization of van der Waals states of ozone. *J. Chem. Phys.* **2011**, *134*, 174308.

(54) Jiang, L.; Babikov, D. A reduced dimensionality model of ozone: Semiclassical treatment of van der Waals states. *Chem. Phys. Lett.* **2009**, *474*, 273–277.

(55) Ivanov, M. V.; Babikov, D. On molecular origin of mass-independent fractionation of oxygen isotopes in the ozone forming recombination reaction. *Proc. Natl. Acad. Sci.* **2013**, *110*, 17708–17713.

(56) Ivanov, M. V.; Grebenshchikov, S. Y.; Schinke, R. Intra- and intermolecular energy transfer in highly excited ozone complexes. *J. Chem. Phys.* **2004**, *120*, 10015–10024.

(57) Dawes, R.; Lolur, P.; Li, A.; Jiang, B.; Guo, H. Communication: An accurate global potential energy surface for the ground electronic state of ozone. *J. Chem. Phys.* **2013**, *139*, 201103.

(58) Tyuterev, V. G.; Kochanov, R. V.; Tashkun, S. A.; Holka, F.; Szalay, P. G. New analytical model for the ozone electronic ground state potential surface and accurate ab initio vibrational predictions at high energy range. *J. Chem. Phys.* **2013**, *139*, 134307.

(59) Dawes, R.; Wang, X.-G.; Carrington Jr, T. CO dimer: new potential energy surface and rovibrational calculations. *J. Phys. Chem. A* **2013**, *117*, 7612–7630.

(60) Brown, J.; Wang, X.-G.; Carrington Jr, T.; Grubbs, G. S.; Dawes, R. Computational study of the rovibrational spectrum of CO_2–CS_2. *J. Chem. Phys.* **2014**, *140*, 114303.

(61) Dawes, R.; Ndengué, S. A. Single- and multireference electronic structure calculations for constructing potential energy surfaces. *Int. Rev. Phys. Chem.* **2016**, *35*, 441–478.

(62) Barclay, A.; McKellar, A.; Moazzen-Ahmadi, N.; Dawes, R.; Wang, X.-G.; Carrington, T. Infrared spectrum and intermolecular potential energy surface of the CO–O_2 dimer. *Phys. Chem. Chem. Phys.* **2018**, *20*, 14431–14440.

(63) Garberoglio, G.; Jankowski, P.; Szalewicz, K.; Harvey, A. H. All-dimensional H2–CO potential: Validation with fully quantum second virial coefficients. *J. Chem. Phys.* **2017**, *146*, 054304.

(64) Gadzhiev, O. B.; Ignatov, S. K.; Kulikov, M. Y.; Feigin, A. M.; Razuvaev, A. G.; Sennikov, P. G.; Schrems, O. Structure, Energy, and Vibrational Frequencies of Oxygen Allotropes On (n $\leq$ 6) in the Covalently Bound and van der Waals Forms: Ab Initio Study at the CCSD(T) Level. *J. Chem. Theory Comput.* **2013**, *9*, 247–262.

(65) Powell, A. D.; Dattani, N. S.; Spada, R. F.; Machado, F. B.; Lischka, H.; Dawes, R. Investigation of the ozone formation reaction pathway: Comparisons of full configuration interaction quantum Monte Carlo and fixed-node diffusion Monte Carlo with contracted and uncontracted MRCI. *J. Chem. Phys.* **2017**, *147*, 094306.

(66) Hippler, H.; Rahn, R.; Troe, J. Temperature and pressure dependence of ozone formation rates in the range 1–1000 bar and 90–370 K. *J. Chem. Phys.* **1990**, *93*, 6560–6569.

(67) Hou, D.; Ma, Y.-T.; Zhang, X.-L.; Li, H. The origins of intra- and intermolecular vibrational couplings: A case study of H_2O–Ar on full and reduced-dimensional potential energy surface. *J. Chem. Phys.* **2016**, *144*, 014301.

(68) Polyansky, O. L.; Ovsyannikov, R. I.; Kyuberis, A. A.; Lodi, L.; Tennyson, J.; Zobov, N. F. Calculation of rotation–vibration energy levels of the water molecule with near-experimental accuracy based on an ab initio potential energy surface. *J. Phys. Chem. A* **2013**, *117*, 9633–9643.

(69) Werner, H.-J.; Knowles, P. J.; Knizia, G.; Manby, F. R.; Schütz, M. Molpro: a general-purpose quantum chemistry program package. *Wil. Inter. Rev.: Comp. Mol. Sc.* **2012**, *2*, 242–253.

(70) Werner, H.-J.; Knowles, P. J.; Knizia, G.; Manby, F. R.; Schütz, M. MOLPRO, version 2015.1, a package of ab initio programs. 2015.

(71) Knizia, G.; Adler, T. B.; Werner, H.-J. Simplified CCSD(T)-F12 methods: Theory and benchmarks. *J. Chem. Phys.* **2009**, *130*, 054104.

(72) Feller, D.; Peterson, K. A.; Crawford, T. D. Sources of error in electronic structure calculations on small chemical systems. *J. Chem. Phys.* **2006**, *124*, 054107.

(73) McCarthy, M. C.; Ndengué, S. A.; Dawes, R. The rotational spectrum and potential energy surface of the Ar–SiO complex. *J. Chem. Phys.* **2018**, *149*, 134308.

(74) Walker, K. M.; Lique, F.; Dawes, R. Fine and hyperfine collisional excitation of C_6H by He. *Mon. Not. R. Astron. Soc.* **2018**, *473*, 1407–1415.

(75) Donoghue, G.; Wang, X.-G.; Dawes, R.; Carrington Jr, T. Computational study of the rovibrational spectra of CO_2–C_2H_2 and CO_2–C_2D_2. *J. Mol. Spectrosc.* **2016**, *330*, 170–178.

(76) Wang, X.-G.; Carrington Jr, T.; Dawes, R. Computational study of the rovibrational spectrum of $(CO_2)_2$. *J. Mol. Spectrosc.* **2016**, *330*, 179–187.

(77) Patkowski, K. On the accuracy of explicitly correlated coupled-cluster interaction energies, have orbital results been beaten yet? *J. Chem. Phys.* **2012**, *137*, 034103.

(78) Sylvetsky, N.; Peterson, K. A.; Karton, A.; Martin, J. M. Toward a W4-F12 approach: Can explicitly correlated and orbital-based ab initio CCSD (T) limits be reconciled? *J. Chem. Phys.* **2016**, *144*, 214101.

(79) Peterson, K. A.; Kesharwani, M. K.; Martin, J. M. The cc-pV5Z-F12 basis set: reaching the basis set limit in explicitly correlated calculations. *Mol. Phys.* **2015**, *113*, 1551–1558.

(80) Shiozaki, T.; Knizia, G.; Werner, H.-J. Explicitly correlated multireference configuration interaction: MRCI-F12. *J. Chem. Phys.* **2011**, *134*, 034113.

(81) Peterson, K. A.; Adler, T. B.; Werner, H.-J. Systematically convergent basis sets for explicitly correlated wavefunctions: The atoms H, He, B–Ne, and Al–Ar. *J. Chem. Phys.* **2008**, *128*, 084102.

(82) Quintas-Sánchez, E.; Dawes, R. AUTOSURF: A Freely Available Program To Construct Potential Energy Surfaces. *J. Chem. Inf. Model.* **2019**, *59*, 262–271.

(83) Dawes, R.; Quintas-Sánchez, E. The Construction of Ab Initio-Based Potential Energy Surfaces. *Rev. Comput. Chem* **2018**, *31*, 199–264.

(84) Dawes, R.; Thompson, D. L.; Guo, Y.; Wagner, A. F.; Minkoff, M. Interpolating moving least-squares methods for fitting potential energy surfaces: Computing high-density potential energy surface data from low-density ab initio data points. *J. Chem. Phys.* **2007**, *126*, 184108.

(85) Dawes, R.; Wang, X.-G.; Jasper, A. W.; Carrington Jr, T. Nitrous oxide dimer: A new potential energy surface and rovibrational spectrum of the nonpolar isomer. *J. Chem. Phys.* **2010**, *133*, 134304.

(86) Guo, Y.; Tokmakov, I.; Thompson, D. L.; Wagner, A. F.; Minkoff, M. Interpolating

moving least-squares methods for fitting potential energy surfaces: Improving efficiency via local approximants. *J. Chem. Phys.* **2007**, *127*, 214106.

(87) Majumder, M.; Ndengue, S. A.; Dawes, R. Automated construction of potential energy surfaces. *Mol. Phys.* **2016**, *114*, 1–18.

(88) Wei, H.; Carrington Jr, T. The triatomic Eckart-frame kinetic energy operator in bond coordinates. *J. Chem. Phys.* **1997**, *107*, 9493–9501.

(89) Wang, X.-G.; Carrington Jr, T. Computing rovibrational levels of methane with curvilinear internal vibrational coordinates and an Eckart frame. *J. Chem. Phys.* **2013**, *138*, 104106.

(90) Meyer, H.-D.; Gatti, F.; Worth, G. A. *Multidimensional quantum dynamics*; John Wiley & Sons, 2009.

(91) Beck, M. H.; Jäckle, A.; Worth, G.; Meyer, H.-D. The multiconfiguration time-dependent Hartree (MCTDH) method: a highly efficient algorithm for propagating wavepackets. *Phys. Rep.* **2000**, *324*, 1–105.

(92) Worth, G.; Beck, M.; Jäckle, A.; Meyer, H.-D. The MCTDH Package, Version 8.2, (2000), University of Heidelberg, Heidelberg, Germany. H.-D. Meyer, Version 8.3 (2002), Version 8.4 (2007), O. Vendrell and H.-D. Meyer, Version 8.5 (2011). 2007; See http://mctdh.uni-hd.de.

(93) Ndengué, S.; Dawes, R.; Gatti, F.; Meyer, H.-D. Atom-triatom rigid rotor inelastic scattering with the MultiConfiguration Time Dependent Hartree approach. *Chem. Phys. Lett.* **2017**, *668*, 42–46.

(94) Gatti, F.; Iung, C. Exact and constrained kinetic energy operators for polyatomic molecules: The polyspherical approach. *Phys. Rep.* **2009**, *484*, 1–69.

(95) Depannemaecker, J.-C.; Bellet, J. Rotational spectra of $^{16}O_3$ and of the five ^{18}O isotopic species. *J. Mol. Spec.* **1977**, *66*, 106–120.

(96) Jäckle, A.; Meyer, H.-D. Product representation of potential energy surfaces. *J. Chem. Phys.* **1996**, *104*, 7974–7984.

(97) Jäckle, A.; Meyer, H.-D. Product representation of potential energy surfaces. II. *J. Chem. Phys.* **1998**, *109*, 3772–3779.

(98) Meyer, H.-D.; Worth, G. A. Quantum molecular dynamics: propagating wavepackets and density operators using the multiconfiguration time-dependent Hartree method. *Theor. Chem. Acc.* **2003**, *109*, 251–267.

(99) Meyer, H.-D.; Le Quéré, F.; Léonard, C.; Gatti, F. Calculation and selective population of vibrational levels with the Multiconfiguration Time-Dependent Hartree (MCTDH) algorithm. *Chem. Phys.* **2006**, *329*, 179–192.

(100) Ndengué, S.; Dawes, R.; Wang, X.-G.; Carrington Jr, T.; Sun, Z.; Guo, H. Calculated vibrational states of ozone up to dissociation. *J. Chem. Phys.* **2016**, *144*, 074302.

(101) Leforestier, C. Grid method for the Wigner functions. Application to the van der Waals system Ar–H_2O. *J. Chem. Phys.* **1994**, *101*, 7357–7363.

(102) Füchsel, G.; Thomas, P. S.; den Uyl, J.; Öztürk, Y.; Nattino, F.; Meyer, H.-D.; Kroes, G.-J. Rotational effects on the dissociation dynamics of CHD_3 on Pt(111). *Phys. Chem. Chem. Phys.* **2016**, *18*, 8174–8185.

(103) Bunker, P. R.; Jensen, P. *Molecular symmetry and spectroscopy*; NRC Research Press, 2006.

(104) DeLeon, R. L.; Mack, K. M.; Muenter, J. Structure and properties of the argon–ozone van der Waals molecule. *J. Chem. Phys.* **1979**, *71*, 4487–4491.